https://doi.org/10.1016/j.clay.2020.105961

Nanoscale Mechanical Behavior of Kaolinite under Uniaxial Strain Conditions

Li-Lan ZHANG[a,b], Yuan-Yuan ZHENG*[a,b], Peng-Chang WEI[a,b], Qiu-Feng DIAO[a,b], Zhen-Yu YIN[c]

a School of Civil Engineering, Sun Yat-Sen University, Guangzhou, 510275, China

b Southern Marine Science and Engineering Guangdong Laboratory (Zhuhai), China

c Department of Civil and Environmental Engineering, The Hong Kong Polytechnic University, Hung Hom, Kowloon, Hong Kong, China

*Corresponding author: Dr. Yuan-Yuan ZHENG, Tel: +86 180 2245 0508;

E-mai: zhengyy57@mail.sysu.edu.cn; zyy378@hotmail.fr

Address: School of Civil Engineering, Zhuhai Campus of SUN Yat-Sen University, Tang Jia Wan, Zhuhai City, P. R. China

Abstract

Nanoscale mechanical behavior of kaolinite as a fundamental failure mechanism has been investigated under uniaxial tension and compression using Molecular Dynamics (MD) simulation methods. External deformation has been applied on kaolinite with a strain rate of 5×10^{-7} fs^{-1} for tensile and compressive tests in the directions parallel (*x*-, *y*-direction)/perpendicular (*z*-direction) to clay mineral layers. Results showed that better mechanical performance was presented in the directions parallel to clay mineral layers than the other direction due to its continuous lattice in this plane. However, the elastic modulus of kaolinite in the *z*-direction was almost half

of that in the other directions, which nearly equals the overall elastic modulus of kaolinite with a value of about 72.6 GPa. Compression in the *x*- and *y*-directions resulted in the separation of clay mineral layers then bending towards the octahedral sheet till crack. Compression in the *z*-direction resulted in slippage of clay mineral layers at the first fracture then resistance till the second fracture at the strain of about 0.2. Tension would cause cracks in the direction perpendicular to the strain direction, which may be a cleavage fracture or cracks in clay mineral sheets. Different failure modes under tension and compression were originated from the layered structure of kaolinite.

Keywords: Molecular dynamics; kaolinite; mechanical behaviors; tension; compression; bending

1 Introduction

Surrounding rocks especially soft rocks easily suffer from deformation or even damage. One major factor is the external force, such as disturbing force in tunnels excavation and petroleum exploitation process. As one of the most abundant clay minerals on the surface of the earth, kaolinite ($Al_2Si_2O_5(OH)_4$) has a wide range of applications, from industrial processes to engineering applications. Clay minerals often play an important role in geohazard origin (Shuzui, 2001; Sierra et al., 2010). Previous studies (Tanaka, 1992; Hicher et al., 1994) demonstrated the existence of many clay minerals with an obvious breakage of both clay particles and aggregates in failure surfaces of shear zones in landslides. Thus, it is of great significance to have a

systematic understanding of the link between the microstructure of clay minerals and their micro-mechanical behaviors under external loads.

So far, a variety of experimental studies on mechanical properties of clay minerals have been investigated in the past two decades (Gridi-Bennadji et al., 2009; Zhang et al., 2009). It was reported that Young's modulus of kaolinite was measured 114 and 117 GPa by indentation at a 2000-nm depth, parallel and perpendicular to clay layers respectively, while 98.4 and 93.3 GPa by ultrasonic echography (Boussois et al., 2013). However, in another indentation work (Han et al., 2018), it was predicted 24.2 and 15.8 GPa on the parallel and vertical bedding plane of pure clay minerals respectively. Without considering anisotropy, much less value of Young's modulus found was 1.3±0.5 GPa for kaolinite macro-crystals (Mikowski et al., 2007). And 6.2 GPa for dickite was first reported by means of the atomic force acoustic microscope (AFAM) (Prasad et al., 2002). Notably, the anisotropy coefficient was found 0.58-0.62 at the nanoscale, 0.56-0.72 at the micro-scale, and 0.7-0.83 at the macro-scale (Han et al., 2018). A remarkable difference among these experimental results may be due to the complex structure of the clay minerals, that the properties of clay mineral aggregates and their particles may be quite different. The experiment results are possibly sensitive to the way of manipulation, the defects of samples such as voids and impurities (Vanorio et al., 2003), as well as the samples' scale. Due to the nanoscale size of clay minerals, it is still difficult to obtain their self-properties by experimental methods, especially their failure behaviors considering structural anisotropy.

Simulations can focus on clay mineral particles themselves. The *Ab initio* method

has been applied to study their mechanical properties (Guimaraes et al., 2010; Scholtzova and Tunega, 2020; Zhao et al., 2020). Molecular dynamic simulation methods have the great advantage of studying the mechanical properties as well as the fracture modes of clay minerals. Large-scale MD simulations of triaxial compression and extension tests (Aminpour and Sjoblom, 2019) have been performed on kaolinite particles (granular matters) to investigate their stress-strain response and strength, which makes it possible to investigate macroscopic mechanical response via the micro-scale method. Deformation occurred mostly in the interlayers instead of clay mineral layers themselves. Linear relationship between applied force and displacement of the interlayer (Katti et al., 2005) has been found when external forces were applied on pyrophyllite. Similar results (Hantal et al., 2014) showed that the lack of chemical bonds between clay layers could cause two failure modes of Illite: the low failure resistance under tension and the stick-slip failure under shear. Therefore, cation exchange capacity in clay minerals (Zartman et al., 2010) and the doping of ions (Zhao et al., 2020) could affect elastic properties by changing ion bonds and layer spacing. Other simulation results showed significant microscopic anisotropy when considering the loading directions (Benazzouz and Zaoui, 2012; Yang et al., 2019). Recently, ManChao He and his team (Yang et al., 2019; Han et al., 2019) has studied the anisotropy of morphological deformation as well as Young's moduli and strengths of kaolinite. Their work focused on the uniaxial tension of kaolinite in the three directions.

Although a great deal of simulation work has been performed to study the anisotropic elastic properties of kaolinite, most of them were obtained through tension

or shear tests. The behavior of kaolinite in compressive mode is still unknown to our best knowledge. However, due to its layered structure, the single-loading method seems not enough to evaluate the comprehensive mechanical properties of kaolinite. To well understand the anisotropic mechanical properties of kaolinite, considering different loading conditions is necessary. Thereafter, to find the relationship between experimental results and the simulation ones is indispensable.

In this paper, uniaxial tension and compression tests on kaolinite in the *x*-, *y*-, and *z*-directions with a controlled strain have been carried out employing the Molecular Dynamics simulation method. The potential failure mechanisms of kaolinite have been discussed. Elastic moduli of kaolinite in different directions, as well as the overall one, have been studied. The relationship between the overall elastic modulus and the anisotropic ones has been investigated at the end.

2 Simulation details

2.1 Modeling

Kaolinite is an anisotropic triclinic crystalline, made up of layers formed of a silica tetrahedral sheet stacking in the [001] direction with an aluminum-oxygen octahedral sheet, as shown in Fig. 1. The lattice parameters of kaolinite are a = 5.154 Å, b = 8.942 Å, c = 7.391 Å, α = 91.93°, β = 105.05°, and γ = 89.80°, obtained by the neutron diffraction method (Bish and Dreele, 1989). To reduce the size effect, a supercell of $12a \times 7b \times 8c$ was built with a dimensionally equal size of 61.848 Å × 62.594 Å × 59.128 Å (672 cells with 22848 atoms) by the software Material Studio, as shown in Fig. 2. The *x*-, *y*-, and *z*-directions are in association with the crystal direction

[100], [010], and [001], respectively.

2.2 Force field

In this work, the atomic interactions of kaolinite were defined according to CLAYFF (Cygan et al., 2004), which includes Van der Waals interactions, electrostatic interactions, and the harmonic bonds of the hydroxyl groups. The Lennard-Jones (LJ) 12-6 potential (Eq. (1)) was used to calculate Van der Waals forces which are the sum of attractive or repulsive interactions between two atoms and the cutoff distance was truncated at 10 Å. The particle mesh Ewald (PME) (Darden et al., 1993) algorithm was applied to treat the electrostatic interactions (Eq. (3)) with the cutoff of 8.5 Å and the Ewald tolerance of 10^{-4}. Eq. (4) was for computing hydrogen bond stretching energy.

$$E_{\mathrm{VDW}} = 4\varepsilon_{ij}\left[\left(\sigma_{ij}/r_{ij}\right)^{12} - \left(\sigma_{ij}/r_{ij}\right)^{6}\right] \quad (1)$$

$$\sigma_{ij} = (\sigma_i + \sigma_j)/2 \ , \ \varepsilon_{ij} = \sqrt{\varepsilon_i \varepsilon_j} \quad (2)$$

$$E_{\mathrm{coul}} = e^2 q_i q_j / (4\varepsilon_0 r_{ij}) \quad (3)$$

$$E_{\mathrm{O\text{-}H}} = k\left(r_{ij} - r_0\right)^2 \quad (4)$$

where σ_{ij} and ε_{ij} are L-J parameters which can be obtained by Lorentz-Berthelot's mixing rules (Eq. (2)) (Frenkel and Smit, 2001); q_i and q_j are the charges of atom *i* and *j* respectively; ε_0 is the dielectric constant, and r_{ij} is the distance between atom *i* and *j*.

2.3 Simulation details

In this study, Molecular Dynamic simulations (MD) have been performed using LAMMPS code (Plimpton, 1995). Periodic boundary conditions were applied to all directions. The Verlet algorithm was used to integrate the motion equation with a

timestep of 1 fs. Both temperature and pressure were controlled by Nosé-Hoover (Hoover, 1985) schemes with a time constant of 100 fs for temperature and 1000 fs for pressure. In addition, pressure coupling was applied independently in the *x*-, *y*-, and *z*-directions. Before performing a series of MD simulations, an equilibrium state of the system at standard ambient conditions (T = 300 K; P = 1 atm) was obtained by applying the first 10 ps simulation with NVT ensemble and then 20 ps simulation with NPT ensemble.

After the relaxation of the initial system, uniaxial tensile and compressive proceeds were achieved by changing the dimension of the simulation box of kaolinite supercell, called a strain-controlled loading approach, applying positive/negative axial strain (corresponding to tension/compression) at a certain rate in different directions.

To evaluate the effect of strain rate on the mechanical behavior of the system, several sets of simulations were performed with different tensile strain rate (10^{-5} fs^{-1}, 5×10^{-6} fs^{-1}, 10^{-6} fs^{-1}, 5×10^{-7} fs^{-1}, 10^{-7} fs^{-1}) in the *x*-direction (parallel to clay mineral layers) and compressive strain rate (-10^{-5} fs^{-1}, -5×10^{-6} fs^{-1}, -10^{-6} fs^{-1}, -5×10^{-7} fs^{-1}, -10^{-7} fs^{-1}) in the *z*-direction (perpendicular to clay mineral layers). The stress-strain curves of these cases during the deformation process are shown in Fig. 3. The deformation rate smaller than 10^{-6} fs^{-1} has little effect on the evolution of stress under both tension and compression, which is consistent with the results in the literature (Yang et al., 2019; Han et al., 2019). Thereafter, the strain-rate of 5×10^{-7} fs^{-1} was chosen in this work to ensure reliability as well as to save computing resources.

In each simulation, the strain load was applied in the axial direction for 600 ps with

a total strain of 0.3. During the simulation, atmospheric pressure was always applied in the other two directions, perpendicular to the strain loading direction. The Open Visualization Tool (OVITO) (Stukowski and Alexander, 2010) was applied to visualize the snapshots of atomic trajectories, as well as to calculate the Radial Distribution Function (RDF) of the system, which helps to illustrate the characteristics of deformation and failure process of kaolinite. Micro-mechanical properties, such as strength, ultimate strain, and anisotropic Young's moduli of kaolinite were analyzed from axial stress-strain curves. The calculated overall elastic modulus was obtained by a series of MD simulations considering all deformation modes and discussed as well.

3 Results and Discussions

3.1 Stress-strain response of tension and compression

In this section, the evolution of axial stress of kaolinite under tension and compression along the *x*-, *y*-, and *z*-directions will be analyzed, as well as their mechanical properties obtained from the stress-strain curves. Note that the *x*- and *y*-directions are parallel to clay mineral layers, while the *z*-direction is in the perpendicular direction. Thus, the deformation pattern of kaolinite in this work can be divided into two types, longitudinal (*z*-direction) and in-plane (*x*- and *y*-direction) deformation.

The trends of axial stress under deformation parallel to clay mineral layers (Fig. 4(a) and (b)) appear similar. However, deformations in the *z*-direction exhibit significant differences in the two loading modes. Comparing the pics of these curves, the tensile and compressive strength of deformations in the *x*- and *y*-directions have a slight difference, while in the *z*-direction the difference is significant. The development

of stress with deformation in the *z*-direction is quite different from that in the *x*- and *y*-directions, which indicates the anisotropic of kaolinite.

The development of stress under tension and compression in the *x*- and *y*-directions (Fig. 4 (a) and (b)) can be divided into three phases (OA, AB and B-). In the first phase (0~2% strain), the stress increases linearly with strain, and thereafter, accelerated or decelerated increases till a peak value (point A). The OA phase can be defined as the elastic-plastic phase. After the peak, the axial stress declines dramatically to a very low value (AB phase), defined as the failure phase. Thereafter, the stress fluctuates slightly around a small value and finally tends to zero (B- phase, called residual phase).

However, the development of stress under compression in the *z*-direction (see curve VI in Fig.4(c)) has different trend compared to that mentioned above. The stress decreases slightly (from A1 to point A2) after the first peak (point A1) and then continues to increase slowly to almost the same value of the first stress peak, followed by a sharp drop and remains a certain stress level.

3.2 Structural Analysis of deformation

In this section, the deformation and failure modes of the atomic structure of kaolinite will be described, which may help to explain the characteristics of axial stress-strain curves. Some representative atomic images corresponding to point A and B marked in stress-strain curves (Fig. 4) are illustrated in Fig. 5. *Tx*-, *Ty*-, and *Tz*- mean the tension in the *x*-, *y*-, and *z*-directions. *Cx*-, *Cy*-, and *Cz*- mean the compression in the *x*-, *y*-, and *z*-directions.

Atoms in images *Tx*-A, *Ty*-A, *Cx*-A, and *Cy*-A in Fig. 5(a) (b) are colored according

198 to their displacements, which shows that the displacement of atoms decreases from the
199 boundary to the interior along the strain direction. At the state of point A, whatever
200 under tension or compression, the system maintains its crystal structure.

201 Images *Tx*-B, *Ty*-B, *Cx*-B, and *Cy*-B in Fig. 5(a) and (b) show the failure state
202 corresponding to point B in the stress-strain curve of Fig. 4. For stretching mode,
203 images *Tx*-B and *Ty*-B, fractures occur in the clay mineral sheets. For compression
204 mode, images *Cx*-B and *Cy*-B, clay mineral layers bend till break as compressive strain
205 accumulates.

206 Some differences appear in terms of cracks orientation between fracture mode
207 along the *x*- or *y*-direction. Tensile cracks occur where the maximum difference of
208 atoms' displacements, just as the dashed line marked in images *Ty*-B. In the case of
209 stretching along the *x*-axis, however, since the system has a 3D boundary condition, the
210 cracks indeed thread together, with an acute-angle between the orientation of the crack
211 and the strain direction. The possible reason may arise from the inclusion angle β =
212 105.05 ° rather than $\gamma \approx 90$ °.

213 Kaolinite layers bend toward the facet of Al-O octahedral sheets under pressure
214 along the *x*- or *y*-direction (Fig. 5, *Cx*-B and *Cy*-B). This is mainly because an original
215 strain exists in the kaolinite lattice due to the mismatch in atomic spacing between the
216 silica tetrahedral sheet and the octahedral sheet, which causes the planar structure to
217 curve with the silica tetrahedral sheet extended and the aluminum octahedral sheet
218 contracted (Singh, 1996; Miller et al., 2007; Li et al., 2015). The bending mode found
219 in this work is also in good agreement with the recently published work (Tunega and

Zaoui, 2020), that Al-O octahedral sheet as the inner surface of the halloysite nanotubes showed better structural stability than the opposite case.

To evaluate whether there is a size effect on the in-plane compressive behaviors or not, two different supercells, 41.232 Å × 44.71 Å × 44.346 Å and 82.464 Å × 80.478 Å × 81.301 Å, have been studied under the same compression condition along the *x*- and *y*-directions. The same bending and fracture modes were found, which means that the size of the periodic cells does not influence the bending mode of the clay mineral structure.

The separation of kaolinite layers was found while bending. The separation energy of the inter-layer as well as the fracture energy of the intra-layer were then studied. The separation energy is defined as the per unit area surface energy. The fracture energy of the intra-layer is defined as the crack energy of damages in octahedra and tetrahedral sheets.

Previous studies (Sakuma, 2013, Sakuma and Suehara, 2015) defined the surface energy as $E_{\mathrm{ILBE}} = \left(E_{2\mathrm{layer}} - 2E_{1\mathrm{layer}}\right)/2A$, where $E_{2\mathrm{layer}}$ is the energy of the system with two stacking layers; $E_{1\mathrm{layer}}$ is the energy of the system with a single layer. As shown in Fig. 6(a), when two single layers stacking together to form a single system, the sum of the energy of two single layers includes twice the energy of the contact surface. Thereafter, the per unit area surface energy of the contact surface should be divided by two.

In this work, the separation energy between kaolinite surfaces is defined as $E_{\mathrm{sep}} = \left(E_2 - E_1\right)/A_1$, where E_1 is the energy of the system with two adjacent layers;

242 E_2 is the energy of the system with two separated layers; A_1 is the contact area of
243 kaolinite in the *xy*-plane, as shown in Fig. 6(b). Since there are always two layers in the
244 studied system before/after separation, the energy difference of these two states is the
245 separation energy of the contact surface. Therefore, it is no need to double the contact
246 area A_1 to obtain the per unit area energy.

247 In order to obtain the system energy E_1, two adjacent layers ($12a \times 7b$) were first
248 built as shown in Fig. 7(a) and then optimized using the steepest descent method in the
249 energy minimization process. Thereafter, taking the final configuration of the adjacent
250 model, the upper layer was then moved 20 Å upwards (Fig. 7(b)), then the system
251 energy E_2 was obtained after the minimization process. The separation energy of
252 kaolinite was obtained as 144 mJ/m^2, which agrees well with the cohesion energy of
253 135 mJ/m^2 (Sakuma and Suehara 2015) and 127 mJ/m^2 (Scholtzová and Tunega, 2020)
254 by the First Principle method.

255 The crack energy is defined as $E_{\text{crack}} = (E_3 - E_2)/A_2$, where E_3 is the energy of
256 the crack system and A_2 is the area of the cut section. To study the crack energy of
257 kaolinite, the layers in Fig. 7(b) were cut along the *x*-direction and then separated over
258 10 Å along the *y*-direction to avoid the interactions between the two portions, as shown
259 in Fig. 7(c). After geometric optimization, the final energy of the crack system E_3 was
260 obtained as 3555 mJ/m^2, which is much higher than the separation one.

261 The small separation energy proved again that the adhesion between adjacent layers
262 of kaolinite is a kind of relatively weak attraction mostly provided through hydrogen
263 bonds, or VDW interactions in the non-compact phase (Fernandez et al., 2011). As a

consequence, kaolinite layers are separated and bend first under compression in the *x*- or *y*-direction, and then crack in the clay mineral sheets as the deformation continues and the energy cumulates.

Due to the "weak link" in the interlayer space, under tension in the direction perpendicular to clay mineral layers, the inter-layer interactions can be easily overcome. As a result, layers are separated quickly (image *Tz*-B) with $\varepsilon_{tf} = 0.059$ just after small movements of the top and bottom layers as shown in image *Tz*-A of Fig. 5(c). On the contrary, the evolution of stress under compression in the *z*-direction indicates that the mechanical property slightly decreases after fracture, and then gradually reinforce till the second fracture. The more compression, the better the mechanical properties. The Radial Distribution Function (RDF) reflects the probability density among two types of the atoms and can reflect the aggregation characteristics of atoms in the system (Douillard et al., 2008), thereafter reflects the atomic distribution characteristics of the system (Zhou et al., 2002). The snapshots of *Cz*-A1, *Cz*-A2, *Cz*-A3, and *Cz*-B in Fig. 5(c) are corresponding to point A1, A2, A3, and B in the stress-strain curve VI of Fig. 4(c), respectively. The total RDF at the initial stage after equilibrium and at the other four compression phases (A1, A2, A3 and B), is shown in Fig. 8. Hydrogen bonds would be formed by the hydroxyls on the octahedra surface and the oxygens on the tetrahedra surface in the condensed phases (Steiner, 2010). Thus, the first, second and third peaks of all the total RDF locate at 1.05 Å, 1.55 Å, and 1.95 Å, correlating to the existence of hydrogen bond, Si-O bond and Al-O bond, respectively. The distribution of the total RDF at point B position (in dark green line) shows a characteristic of short-range order

and long-range disorder, different from the other cases. Combined with the snapshots in Fig. 5(c), RDF curves indicate that the crystal structure of kaolinite is not yet broken in phase from A1 to A3. The small decline of stress between phases A1 and A2 may be due to the reorganization of the atomic structure of kaolinite. Further analysis is carried out via the snapshots of the displacement distribution along the *x*- and *y*-directions at point A1 and A2 (images *Cz*-A1-*Sx*–*Sy* and *Cz*-A2–*Sx*–*Sy*). The non-uniform lateral offset of adjacent layers indicates that obvious stacking faults occur in A1 and A2 phases. After slippage, the continuous compressive strain can further compact clay mineral layers (snapshot *Cz*-A3) up to structural disorder and yield (snapshot *Cz*-B).

Overall, there are five stages of the compression of kaolinite in the *z*-direction: preliminary compaction (phase O-A1), layer slipping (phase A1-A2), further compaction (phase A2-A3), failure (phase A3-B), and residual stage (phase B-). However, for other cases shown in Fig. 4, phase A-B reflects fractures that may be crack or bending in clay mineral layers.

3.3 Mechanical properties

The peak of stress with its corresponding strain in a stress-strain curve is usually considered as ultimate strength and fracture strain, which is marked as point A in each curve (see Fig. 4). Residual strength can be calculated from the mean stress in a segment with the strain range from 0.22 to 0.3. Table 1 collected the tensile strength σ_{tf}, compressive strength σ_{cf}, peak strain $\varepsilon_{\mathrm{tf}}$, and $\varepsilon_{\mathrm{cf}}$, as well as the residual strength of tension and compression. In all cases the residual strength can be negligible, except the case under compression in the *z*-direction, exhibiting a value of 4.31 GPa. The tensile

strengths of kaolinite are 11.03, 12.70, and 1.81 GPa along the *x*-, *y*-, and *z*-directions respectively, which agree well with the results of 10.2, 12.2, 1.7 GPa from other MD simulations (Yang et al. 2019). The compressive strengths found are 15.49, 10.86, and 14.39 GPa along the *x*-, *y*-, and *z*-directions. To the best of our knowledge, the atomic-scale compressive strengths of kaolinite have not yet reported, so that our simulation results will be a prediction. The different behavior of tension and compression of kaolinite in the three directions indicates that the layer structure is insensitive to its compressive properties but sensitive to its tensile properties. In the direction perpendicular to clay mineral layers, the tensile strength found is inferior to 2 GPa with corresponding strain inferior to 0.06. However, in the direction parallel to clay mineral layers, the tensile strength is found over 10 GPa with a corresponding strain of about 0.1. On the other hand, the difference between σ_{tf} and σ_{cf} in the *x*-direction is only about 30%, and that in the *y*-direction is about 15%.

Thus, the results indicate that no significant difference is found for the mechanical properties of kaolinite in the directions parallel to clay mineral layers under both tension and compression. However, the anisotropic of kaolinite is reflected not only in the weakness of mechanical properties in the direction perpendicular to clay mineral layers, but also in the extremely different behavior of tension and compression in this direction. These mechanical characteristics may be due to its structural characteristics, which are continuous in the clay mineral layer formed by Al-center octahedra and Si-center tetrahedra but lamellar with hydrogen bonding in the perpendicular direction (see Fig. 2).

Indeed, clay minerals usually exist in the form of clay particles. The elastic properties of kaolinite particles should be paid more attention to under certain circumstances especially in geo-engineering. To our knowledge, only the experimental and theoretical results of overall elastic properties of kaolinite have been reported so far (Wang et al., 2001; Vanorio et al., 2003; Sato et al., 2005; Wenk et al., 2008; Weck et al., 2015). Simulated values in the micro-scale should be needed for further verification. What we attempt to study in this section is to evaluate the anisotropic and overall Young's moduli of kaolinite through comprehensive consideration of all deformation forms, trying to find their relationship.

In view of anisotropy, Young's modulus, according to Hooke's law, is calculated from the slope of 0-2% strain in the stress-strain curve shown in Fig. 4, where the stress showed linearity with the axial strain. The linear fitting results with fitting errors are shown in Table 2, together with the mean Young's modulus E of three directions, which are acquired by calculating the average of tension and compression simulation results.

The mean longitudinal modulus (in the z-direction) is almost half of the transverse ones (in the x- and y-directions). The values in the x- and y-directions are very close. This indicates that the difference in the arrangement of atoms (see Fig. 1) in the layer plane has little effect on stiffness. The longitudinal results differ greatly from the other two strain states, which can be attributable to the discontinuity in the layer structure.

The overall elastic properties of kaolinite are obtained by calculating the elastic constants under different deformation conditions. First, a couple of ±2% strain was applied successively to the equilibrated system mentioned before in the six directions

(*x*, *y*, *z*, *xy*, *yz*, *xz*), resulting in 12 deformed cells. Thereafter, a relaxation procedure of 10 ps was performed on these deformed cells to achieve their equilibrium states, in which the cell parameters and six pressure components of these deformed models were then recorded. At last, the elastic constants were recorded as $\mathbf{C}_{ij}$ listed in Table 3 by calculating the average of positive and negative pressure tensors. Comparing the elastic constants of kaolinite in three principal planes, c_{11} (195.69 GPa) is very close to c_{22} (204.69 GPa) with a deviation of less than 0.5%. The smallest is c_{33} at 77.08 GPa, as expected. The elastic constants found in this work are close to the other theoretical and experimental results.

Then, the Voigt–Reuss–Hill model (Hill, 1952) was applied to calculate the elastic properties of kaolinite including Young's modulus E, bulk modulus K, shear modulus G, and Poisson's ratio υ, shown in Table 3. The bulk and shear modulus of kaolinite found in this work were 63.96 and 27.69 GPa respectively, which is comparable with other theoretical and experimental results. The great difference between different experimental results may be due to the experimental methods, that the fracture of the kaolinite sample occurred in the clay mineral layers or in the interlayer would lead to different results. Poisson's ratio in this work was found as 0.311, which agrees well with other results.

The overall Young's modulus found as 72.60 GPa in this work, is within the interval of 72~78 GPa for the modulus in the *z*-direction (see in Table 2). Combined with the poor tensile properties in the *z*-direction mentioned above, it can be argued that the lamellar hydrogen bonding is the "weak link" in kaolinite, which weakens both the

overall mechanical and the elastic properties.

4 Conclusions

This work presented a systematic MD study of deformation and failure behavior of kaolinite at atomic scale under tension and compression in the three principal directions. Stretching in the *x*- and *y*-directions can lead to cracks in clay mineral layers, which is due to the fracture of octahedral and tetrahedral sheets, so the mechanical properties found may be very high. Stretching in the *z*-direction can cause cleavage fracture, which is due to the decohesion in the interlayer space, so the mechanical properties found may be relatively weak. Compression in the *x*- and *y*-directions can lead to layer separation then bending till fracture. Compression in the *z*-direction may result in layer slippage at the first fracture to reorganize the atomic structure and to form further hydrogen bonds between approaching layers, thereafter the deformed structure can resist till the second fracture at the strain of about 0.2.

Slight differences were found between the mechanical properties of kaolinite in the *x*- and *y*-directions because of the continuous hexagonal array of tetrahedra and octahedra along with layers. The overall elastic modulus approximately equaled the weakest one in the three directions with a value of about 72.6 GPa, which is nearly half of the plane ones (*x*- or *y*-direction).

Acknowledgements

This research was financially supported by the National Natural Science

Foundation of China (Grant No. 52009149) and the Research Grants Council (RGC) of Hong Kong Special Administrative Region Government (HKSARG) of China (Grant No.: 15217220).

References

Aminpour, P. and Sjoblom, K. 2019. Multi-Scale Modelling of Kaolinite Triaxial Behaviour. Géotech. Lett. 9, 178-185. doi:10.1680/jgele.18.00194

Benazzouz, B. K. and Zaoui A. 2012. A nanoscale simulation study of the elastic behaviour in kaolinite clay under pressure. Mater. Chem. Phys. 132, 880-888. doi: 10.1016/j.matchemphys.2011.12.028

Bish, David and Dreele, R. B. 1989. Rietveld Refinement of Non-Hydrogen Atomic Positions in Kaolinite. Clay. Clay Miner. 37, 289-296. doi:10.1346/CCMN.1989.0370401

Boussois, K., S. Deniel, N. Tessier-Doyen, D. Chateigner, C. Dublanche-Tixier and P. Blanchart. 2013. Characterization of textured ceramics containing mullite from phyllosilicates. Ceram. Int. 39, 5327-5333. doi:10.1016/j.ceramint.2012.12.038

Cygan, Randall T., Jian-Jie Liang and Andrey G. Kalinichev. 2004. Molecular Models of Hydroxide, Oxyhydroxide, and Clay Phases and the Development of a General Force Field. J. Phys. Chem. B. 108, 1255-1266. doi:10.1021/jp0363287

Darden, Tom, Darrin York and Lee Pedersen. 1993. Particle mesh Ewald: An N · log (N) method for Ewald sums in large systems. J. Chem. Phys. 98,10089-10092.

Douillard, J. M., S. Lantenois, B. Prelot, J. Zajac and M. Henry. 2008. Study of the

417 influence of location of substitutions on the surface energy of dioctahedral
418 smectites. J. Colloid Interf. Sci. 325, 275-281. doi:10.1016/j.jcis.2008.05.012
419 Fernandez, Rodrigo, Fernando Martirena and Karen L. Scrivener. 2011. The origin of
420 the pozzolanic activity of calcined clay minerals: A comparison between kaolinite,
421 illite and montmorillonite. Cement Concrete Res. 41, 113-122.
422 doi:10.1016/j.cemconres.2010.09.013
423 Frenkel, Daan and Berend Smit. 2001. Understanding molecular simulation: From
424 algorithms to applications. Academic Press.
425 Gridi-Bennadji, F., Chateigner, D., Vita, G. Di and Blanchart, P. 2009. Mechanical
426 properties of textured ceramics from muscovite–kaolinite alternate layers. J. Eur.
427 Ceram. Soc. 29, 2177-2184. doi:10.1016/j.jeurceramsoc.2009.01.004
428 Guimarães, Luciana, Andrey N. Enyashin, Gotthard Seifert and Hélio A. Duarte. 2010.
429 Structural, Electronic, and Mechanical Properties of Single-Walled Halloysite
430 Nanotube Models. J. Phys. Chem. C. 114, 11358-11363. doi:10.1021/jp100902e
431 Han, Qiang, Zhan Qu and Zhengyin Ye. 2018. Research on the mechanical behaviour
432 of shale based on multiscale analysis. Roy. Soc. Open Sci. 5, 181039.
433 doi:10.1098/rsos.181039
434 Hantal, György, Laurent Brochard, Hadrien Laubie, Davoud Ebrahimi, Roland J-M
435 Pellenq, Franz-Josef Ulm and Benoit Coasne. 2014. Atomic-scale modelling of
436 elastic and failure properties of clays. Mol. Phys. 112, 1294-1305.
437 doi:10.1080/00268976.2014.897393
438 Hicher, P. Y., Wahyudi, H. and Tessier, D. 1994. Microstructural analysis of strain

localisation in clay. Comput. Geotech. 16, 205-222. doi:10.1016/0266-352X(94)90002-7

Hill, R. 1952. The Elastic Behaviour of a Crystalline Aggregate. Proc. Phys. Soc., A. 65, 349-354. doi:10.1088/0370-1298/65/5/307

Hoover, William G. 1985. Canonical dynamics: Equilibrium phase-space distributions. Phys. Rev. A. 31, 1695-1697. doi:10.1103/PhysRevA.31.1695

Katahara K. W. 1996. Clay mineral elastic properties. SEG Technical Program Expanded Abstracts 1996, Society of Exploration Geophysicists. pp. 1691-1694.

Katti, Dinesh R., Steven R. Schmidt, Pijush Ghosh and Kalpana S. Katti. 2005. Modeling the response of pyrophyllite interlayer to applied stress using steered molecular dynamics. Clay. Clay Miner. 53, 171-178. doi:10.1346/CCMN.2005.0530207

Li, Xiaoguang, Qinfu Liu, Hongfei Cheng, Shuai Zhang and Ray L. Frost. 2015. Mechanism of kaolinite sheets curling via the intercalation and delamination process. J. Colloid Interf. Sci. 444, 74-80. doi:10.1016/j.jcis.2014.12.039

Mikowski, A., P. Soares, F. Wypych, J. E. F. C. Gardolinski and Cm Lepienski. 2007. Mechanical properties of kaolinite 'macro-crystals'. Philos. Mag. 87, 4445-4459. doi:10.1080/14786430701550394

Militzer, B., Wenk, H. R., Stackhouse, S. and Stixrude, L. 2011. First-principles calculation of the elastic moduli of sheet silicates and their application to shale anisotropy. Am. Mineral. 96, 125-137. doi:10.2138/am.2011.3558

Miller, Jan D., Jakub Nalaskowski, Baseer Abdul and Hao Du. 2007. Surface

461 Characteristics of Kaolinite and Other Selected Two Layer Silicate Minerals. Can.
462 J. Chem. Eng. 85, 617-624. doi:10.1002/cjce.5450850508
463 Plimpton, Steve. 1995. Fast Parallel Algorithms for Short-Range Molecular Dynamics.
464 J. Comput. Phys. 117, 1-19. doi:10.1006/jcph.1995.1039
465 Prasad, Manika, Malgorzata Kopycinska, Ute Rabe and Walter Arnold. 2002.
466 Measurement of Young's modulus of clay minerals using atomic force acoustic
467 microscopy. Geophys. Res. Lett. 29, 11-13. doi:10.1029/2001GL014054
468 Sakuma, Hiroshi. 2013. Adhesion energy between mica surfaces: Implications for the
469 frictional coefficient under dry and wet conditions. J. Geophys. Res. 118, 6066-
470 6075. doi:10.1002/2013JB010550
471 Sakuma, Hiroshi and Shigeru Suehara. 2015. Interlayer bonding energy of layered
472 minerals: Implication for the relationship with friction coefficient. J. Geophys. Res.
473 120, 2212-2219. doi:10.1002/2015JB011900
474 Sato, Hisako, Kanta Ono, Cliff T. Johnston and Akihiko Yamagishi. 2005. First-
475 principles studies on the elastic constants of a 1:1 layered kaolinite mineral. Am.
476 Mineral. 90, 1824-1826. doi:10.2138/am.2005.1832
477 Scholtzová, Eva and Daniel Tunega. 2020. Prediction of mechanical properties of
478 grafted kaolinite – A DFT study. Appl. Clay Sci. 193, 105692.
479 doi:10.1016/j.clay.2020.105692
480 Shuzui, Haruo. 2001. Process of slip-surface development and formation of slip-surface
481 clay in landslides in Tertiary volcanic rocks, Japan. Eng. Geol. 61, 199-220.
482 doi:10.1016/S0013-7952(01)00025-4

Sierra, R., Tran, M. H., Abousleiman, Y. N. and Slatt, R. M. 2010. Woodford Shale Mechanical Properties And the Impacts of Lithofacies. In 44th U.S. Rock Mechanics Symposium and 5th U.S.-Canada Rock Mechanics SymposiumSalt Lake City, Utah: American Rock Mechanics Association. doi:10.1023/A:1026727406053

Singh, Balbir. 1996. Why Does Halloysite Roll?—A New Model. Clay. Clay Miner. 44, 191-196. doi:10.1346/CCMN.1996.0440204

Steiner, T. 2010. The Hydrogen Bond in the Solid State. Angew. Chem. Int. Edit. 41, 48-76. doi:10.1002/1521-3773(20020104)41:1<48::AID-ANIE48>3.0.CO;2-U

Stukowski and Alexander. 2010. Visualization and analysis of atomistic simulation data with OVITO–the Open Visualization Tool. Modelling Simul. Mater. Sci. Eng. 18, 015012. doi:10.1088/0965-0393/18/1/015012

Tanaka, K. 1992. Slope hazards and clay minerals. J. Clay Sci. Sco. Japan (in Japanese). 32, 16-22. doi:10.11362/jcssjnendokagaku1961.32.16

Tunega, Daniel and Ali Zaoui. 2020. Mechanical and Bonding Behaviors Behind the Bending Mechanism of Kaolinite Clay Layers. J. Phys. Chem. C. 124, 7432-7440. doi:10.1021/acs.jpcc.9b11274

Vanorio, Tiziana, Manika Prasad and Amos Nur. 2003. Elastic properties of dry clay mineral aggregates, suspensions and sandstones. Geophys. J. Int. 155, 319-326. doi:10.1046/j.1365-246X.2003.02046.x

Wang, Zhijing Zee, Hui Wang and Michael E. Cates. 2001. Effective elastic properties of solid clays. Geophysics. 66, 428-440. doi:10.1190/1.1444934

505 Weck, Philippe F., Eunja Kim and Carlos F. Jové-Colón. 2015. Relationship between
506 crystal structure and thermo-mechanical properties of kaolinite clay: beyond
507 standard density functional theory. Dalton T. 44, 12550-12560.
508 doi:10.1039/c5dt00590f
509 Wenk, H. R., M. Voltolini, M. Mazurek, L. R. Van Loon and A. Vinsot. 2008. Preferred
510 orientations and anisotropy in shales: Callovo-Oxfordian shale (France) and
511 Opalinus Clay (Switzerland). Clay. Clay Miner. 56, 285-306.
512 doi:10.1346/CCMN.2008.0560301
513 Yang, Hua, ManChao He, ChunSheng Lu and WeiLi Gong. 2019. Deformation and
514 failure processes of kaolinite under tension: Insights from molecular dynamics
515 simulations. Sci. China-Phys. Mech. Astron. 62, 64612. doi:10.1007/s11433-018-
516 9316-3
517 Zartman, Gregory D., Hua Liu, Brahim Akdim, Ruth Pachter and Hendrik Heinz. 2010.
518 Nanoscale Tensile, Shear, and Failure Properties of Layered Silicates as a Function
519 of Cation Density and Stress. J. Phys. Chem. C. 114, 1763-1772.
520 doi:10.1021/jp907012w
521 Zhang, Guoping, Zhongxin Wei and Ray E. Ferrell. 2009. Elastic modulus and hardness
522 of muscovite and rectorite determined by nanoindentation. Appl. Clay Sci. 43,
523 271-281. doi:10.1016/j.clay.2008.08.010
524 Zhao, Jian, Xinzhan Qin, Jiamin Wang and Manchao He. 2020. Effect of Mg(II) and
525 Na(I) Doping on the Electronic Structure and Mechanical Properties of Kaolinite.
526 Minerals-Basel. 10, 368. doi:10.3390/min10040368

527 Zhou, Jian, Xiaohua Lu, Yanru Wang and Jun Shi. 2002. Molecular dynamics study on
528 ionic hydration. Fluid Phase Equilibr. 194, 257-270. doi:10.1016/S0378-
529 3812(01)00694-X
530 Zongfang, Han, Yang Hua and He Manchao. 2019. A molecular dynamics study on the
531 structural and mechanical properties of hydrated kaolinite system under tension.
532 Mater. Res. Express. 6, 0850c3. doi:10.1088/2053-1591/ab2562
533

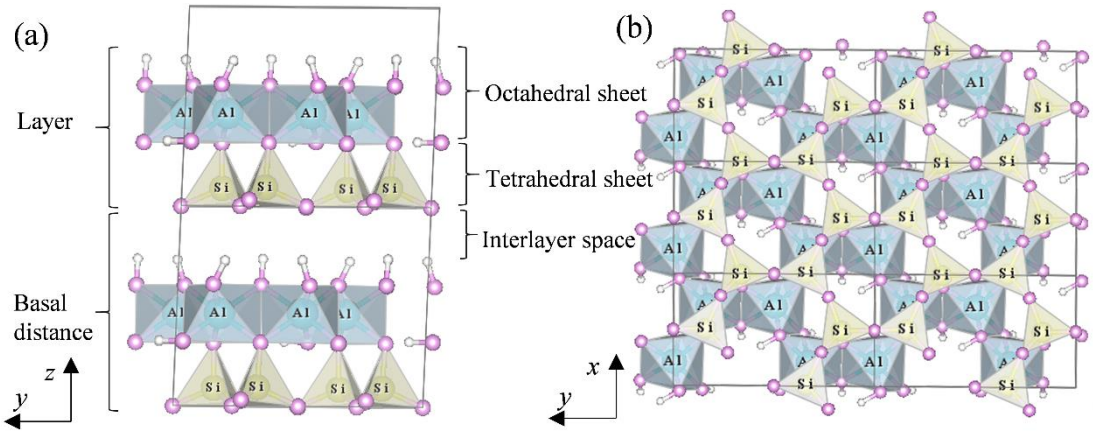

534

535 **Fig. 1:** Crystal structure of kaolinite (a) view from *x*-axes; (b) in-plane ring network

536 formed by six Al-O octahedra and six Si-O tetrahedra, view from *z*-axes. (Al - blue, Si

537 - yellow, O - purple, and H - white)

538

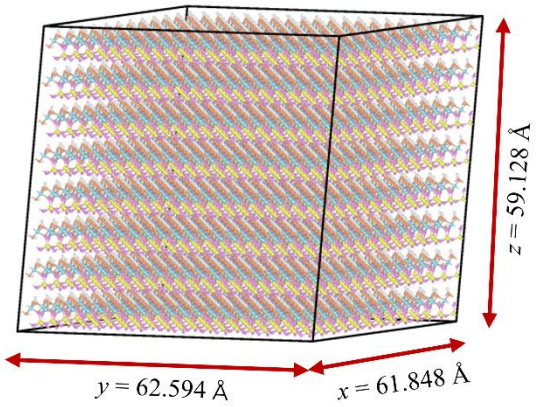

539

540 **Fig. 2:** A $12a \times 7b \times 8c$ kaolinite supercell applied in this work

541

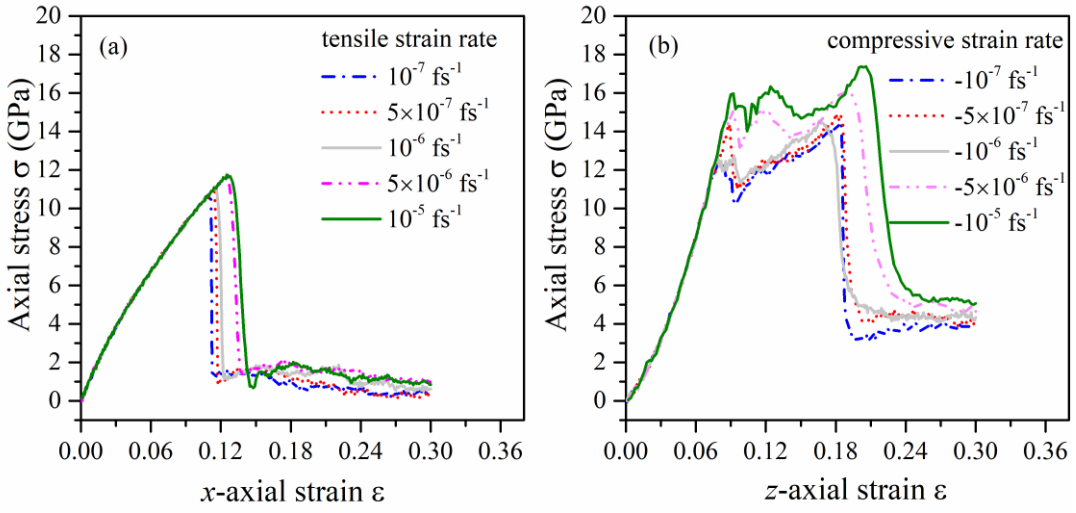

542

543 **Fig. 3:** The axial stress-strain (σ-ε) relationships for Kaolinite with different strain rates:

544 (a) under tension in the *x*-direction; (b) under compression in the *z*-direction.

545

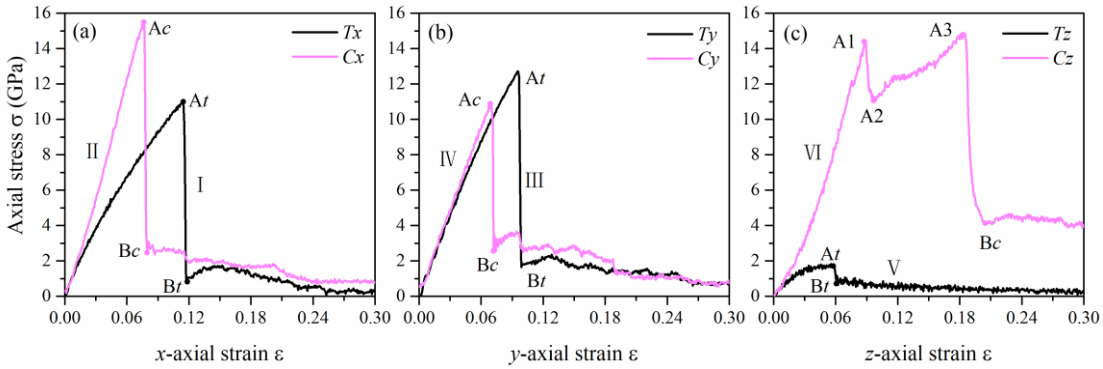

546

547 **Fig. 4:** The axial stress-strain (σ-ε) relationships for kaolinite under tension and

548 compression in the (a) *x*-, (b) *y*- and (c) *z*-direction with a fixed strain rate of 5×10^{-7} fs^{-1}.

549 *Tx*, *Ty*, and *Tz* for tension in the *x*-, *y*-, and *z*-directions respectively. *Cx*, *Cy*, and *Cz* for

550 compression in the *x*-, *y*-, and *z*-directions respectively; the subscript *t* for tension case;

551 the subscript *c* for compression case.

552

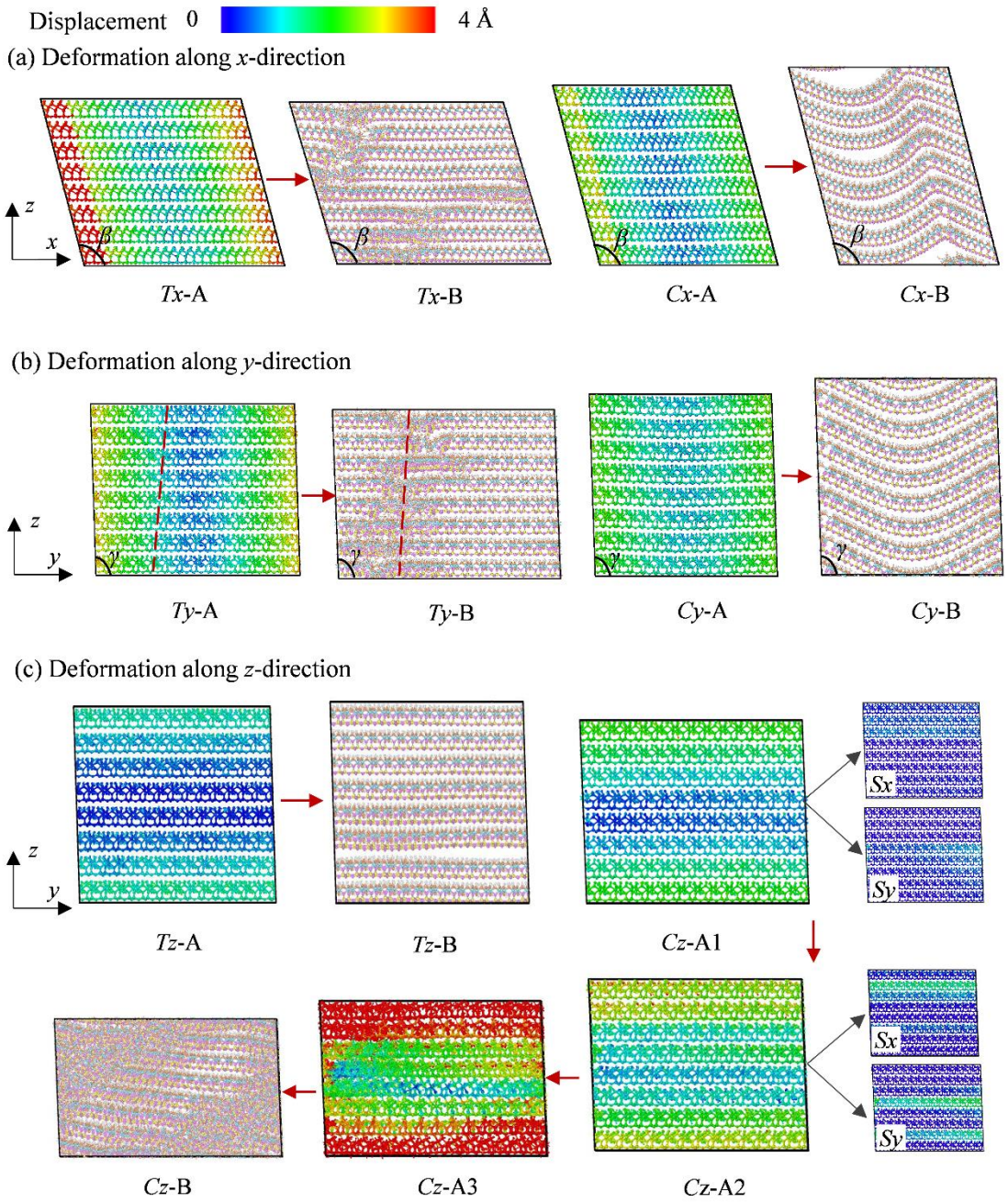

553

554 **Fig. 5:** Snapshot of deformation of kaolinite under tension and compression along the

555 (a) *x*-, (b) *y*-, and (c) *z*-directions. *Tx*: tension along the *x*-direction; *Cy*: compression

556 along the *y*-direction; *Sx*: atomic displacement along the *x*-direction. Point A, B, A1,

557 A2, and A3 correspond to the states marked in the curves of **Fig. 4**. Displacement scale

558 is 0 ~ 4 Å, with the color changes from dark blue, through green to red.

559

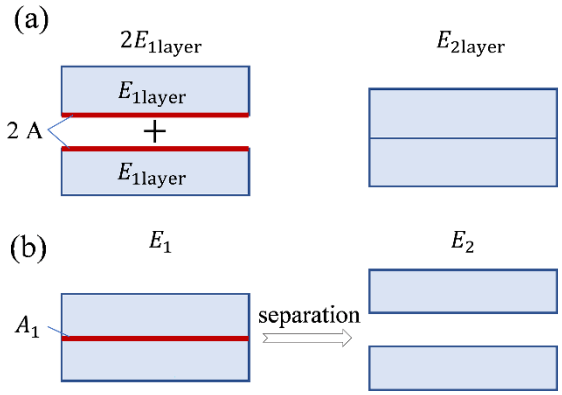

560

561 **Fig. 6:** Schematic diagram for the calculation of (a) the interlayer bonding energies in

562 reference (Sakuma and Suehara, 2015) and (b) the separation energy in this work.

563

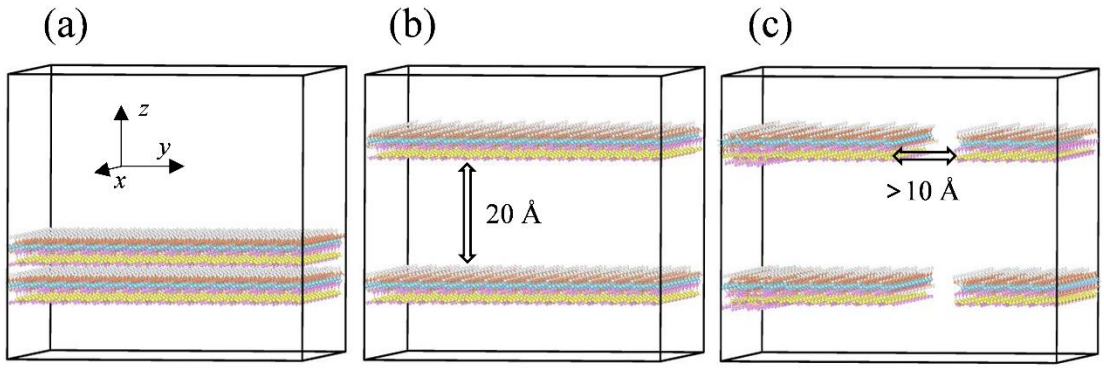

564

565 **Fig. 7:** Schemas of different states (a) initial state; (b) interlayer separation; (c) broken

566 sheets to study the separation and the fracture energy of clay mineral.

567

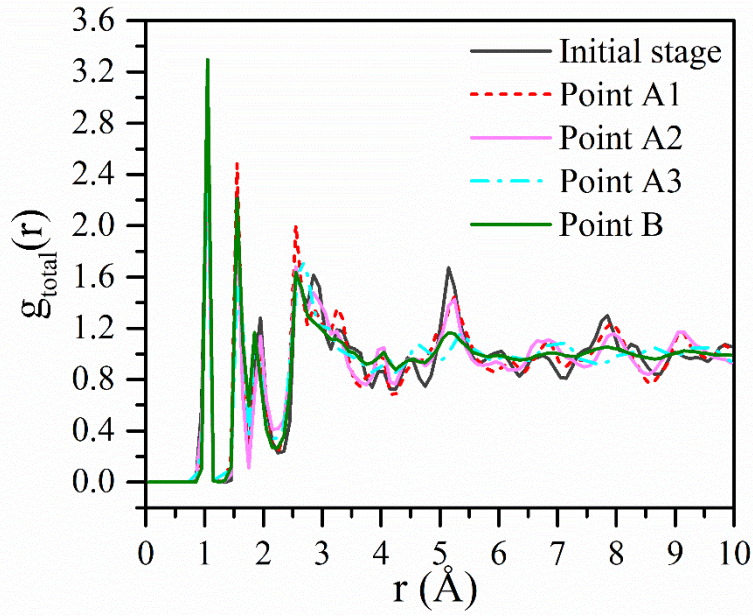

568

569 **Fig. 8:** The total Radial Distribution Functions (RDF) of kaolinite at several

570 representative stages under uniaxial compression along the *z*-direction.

571

572 **Table 1:** Mechanical properties of kaolinite under tension and compression in the

573 *x*-, *y*-, and *z*-directions.

Direction	*x*	*y*	*z*
Ultimate tensile strength σ_{tf} (GPa)	11.03	12.70	1.81
Ultimate compressive strength σ_{cf} (GPa)	15.49	10.86	14.39
Fracture tensile strain ε_{tf}	0.114	0.096	0.059
Fracture compressive strain ε_{tf}	0.077	0.069	0.088
Residual tensile strength (GPa)	0.41	1.01	0.31
Residual compressive strength (GPa)	0.91	0.92	4.31

574

575

576

577

578 **Table 2:** Anisotropic Young's Modulus of kaolinite obtained from stress-strain curves

579 and other DFT results. (in GPa)

Direction	*x*	*y*	*z*
Tensile Young' Modulus E_t	139±3	166±5	58±3
Compressive Young's Modulus E_c	173±3	157±5	95±3
Mean Young's Modulus E	153~159	157~167	72~78
DFT (Weck et al., 2015)	160.85	155.61	85.89
DFT-D2 (Weck et al., 2015)	154.20	148.54	125.42

580

581

582 **Table 3:** Elastic constants and overall elastic properties of kaolinite (in GPa). K is

583 bulk modulus, G is shear modulus, υ is Poisson's Ratio and E is Young's

584 modulus.

C_{ij}	This work	First-principles studies					Experiments		GULP
		a	b	c	d	e	f	g	h
c_{11}	195.69	178.5 ± 8.8	166.0	187.20	177.8	139.18	171.51	94.8-126.4	249.12
c_{12}	93.73	71.5 ± 7.1	64.8	66.42	63.5	52.46			124.82
c_{13}	3.62	2.0 ± 5.3	16.0	15.63	14.1	28.30	27.11	8.5-13.1	14.52
c_{14}	2.55	−0.4 ± 2.1	0.0	-0.74	-7.3	-4.50			6.40
c_{15}	3.92	−41.7 ± 1.4	−37.2	1.18	2.7	-35.78			0.08
c_{16}	-3.14	−2.3 ± 1.7	−7.2	-6.14	-1.2	-4.50			-0.85
c_{22}	204.69	200.9 ± 12.8	177.8	180.20	174.7	170.20			259.22
c_{23}	5.77	−2.9 ± 5.7	11.2	16.00	13.5	11.72			18.72
c_{24}	3.05	−2.8 ± 2.7	−3.3	-0.30	0.2	-7.30			5.69
c_{25}	0.03	−19.8 ± 0.6	−16.2	-0.04	3.4	-14.50			1.44
c_{26}	8.50	1.9 ± 1.5	−0.8	0.58	-2.5	-25.55			6.42
c_{33}	77.08	32.1 ± 2.0	70.1	88.02	107.1	45.50	52.62	57.8-90.9	52.09
c_{34}	-0.12	−0.2 ± 1.4	−1.3	-0.96	0.9	-3.72			1.57
c_{35}	0.76	1.7 ± 1.8	1.3	-0.56	-0.6	-4.46			-4.15
c_{36}	5.02	3.4 ± 2.2	0.2	0.37	-5.8	3.86			-0.64

c_{44}	7.90	11.2 ± 5.6	13.4	9.63	15.5	9.66	14.76	31.6-38.8	12.48
c_{45}	-2.28	−1.2 ± 1.2	0.1	-0.45	-0.2	-1.25			-0.17
c_{46}	-0.89	−12.9 ± 2.4	−14.2	-1.2	0.2	-13.18			-1.03
c_{55}	8.21	22.2 ± 1.4	21.7	13.36	11.8	18.62			16.03
c_{56}	-0.31	0.8 ± 0.7	0.6	-0.02	-1.7	2.75			-1.05
c_{66}	60.37	60.1 ± 3.2	56.7	62.10	61.6	53.60	66.31	40.8-53.6	66.65
K	63.96	23	47.9[i]	65.82	67.8	44.001	56		44.85
G	27.69		19.7[i]	30.79	36.1	22.552	31.8		24.11
v	0.311	0.352	0.319[i]	0.298-0.317	0.3	0.281	0.301	0.022-0.592	0.272
E	72.60		51.97[i]		91.6	57.783			

a- Sato et al., 2005; b- Militzer et al., 2011; c- Weck et al., 2015;

d- Scholtzova and Tunega, 2020; e- Zhao et al., 2020; f- Katahara, 1996;

g- Wenk et al., 2008; h- Benazzouz and Zaoui, 2012; i- Wang et al., 2001.